

See discussions, stats, and author profiles for this publication at: <https://www.researchgate.net/publication/230828045>

# Binder-Free and Carbon-Free Nanoparticle Batteries: A Method for Nanoparticle Electrodes without Polymeric Binders or Carbon Black

ARTICLE *in* NANO LETTERS · SEPTEMBER 2012

Impact Factor: 13.59 · DOI: 10.1021/nl3019559 · Source: PubMed

---

CITATIONS

50

---

READS

154

## 3 AUTHORS:



[Don-Hyung Ha](#)

Massachusetts Institute of Technology

14 PUBLICATIONS 263 CITATIONS

[SEE PROFILE](#)



[Mohammad Anwarul Islam](#)

State University of New York at Oswego

28 PUBLICATIONS 508 CITATIONS

[SEE PROFILE](#)



[Richard D Robinson](#)

Cornell University

61 PUBLICATIONS 2,561 CITATIONS

[SEE PROFILE](#)

# Binder-Free and Carbon-Free Nanoparticle Batteries: A Method for Nanoparticle Electrodes without Polymeric Binders or Carbon Black

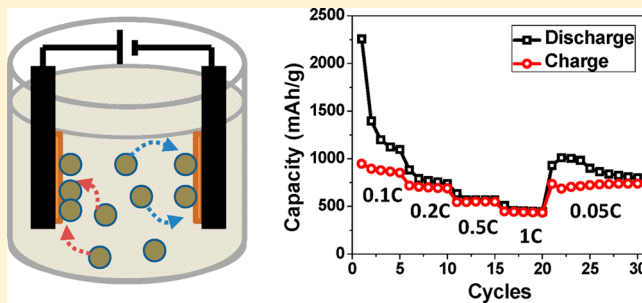
Don-Hyung Ha, Mohammad A. Islam, and Richard D. Robinson\*

Department of Materials Science and Engineering, Cornell University, Ithaca, New York 14853, United States

 Supporting Information

**ABSTRACT:** In this work, we have developed a new fabrication method for nanoparticle (NP) assemblies for Li-ion battery electrodes that require no additional support or conductive materials such as polymeric binders or carbon black. By eliminating these additives, we are able to improve the battery capacity/weight ratio. The NP film is formed by using electrophoretic deposition (EPD) of colloidally synthesized, monodisperse cobalt NPs that are transformed through the nanoscale Kirkendall effect into hollow  $\text{Co}_3\text{O}_4$ . EPD forms a network of NPs that are mechanically very robust and electrically connected, enabling them to act as the Li-ion battery anode. The morphology change through cycles indicates stable 5–10 nm NPs form after the first lithiation remained throughout the cycling process. This NP-film battery made without binders and conductive additives shows high gravimetric ( $>830 \text{ mAh/g}$ ) and volumetric capacities ( $>2100 \text{ mAh/cm}^3$ ) even after 50 cycles. Because similar films made from drop-casting do not perform well under equal conditions, EPD is seen as the critical step to create good contacts between the particles and electrodes resulting in this significant improvement in battery electrode assembly. This is a promising system for colloidal nanoparticles and a template for investigating the mechanism of lithiation and delithiation of NPs.

**KEYWORDS:** Nanoparticle, cobalt oxide, electrophoretic deposition, Li-ion battery electrode, binder-free and carbon-free



Nanoscale materials are extensively investigated and implemented for Li-ion battery electrodes due to their high surface-to-volume ratio and reduced Li-ion diffusion length, which results in faster charge/discharge.<sup>1–3</sup> Nanomaterials also show the ability to accommodate strain through volume expansion without pulverization or capacity fading.<sup>2</sup> In particular, nanoscale transition metal oxides have been studied as alternative anode materials due to their high capacity, as demonstrated by Tarascon et al.<sup>1</sup> The mechanism for lithiation/delithiation in these particles is through the formation and decomposition of  $\text{Li}_2\text{O}$ .<sup>1,3</sup> Similar schemes have been expanded to various other transition metal oxides such as  $\text{Fe}_3\text{O}_4$ ,  $\text{Fe}_2\text{O}_3$ ,  $\text{Co}_3\text{O}_4$ ,  $\text{SnO}_2$ , and  $\text{Mn}_3\text{O}_4$  leading to improved energy densities and high power density beyond bulk values.<sup>1,4,5</sup>

However, understanding the physical mechanisms of these advances is obfuscated by inhomogeneities routinely introduced in battery construction, such as the addition of carbon-based conductive materials and polymeric binders, and the polydisperse size distribution of the particles. The commonly used carbon or acetylene black and polymeric binders are included for electrical conduction and better physical contacts between particles and current collector, respectively.<sup>6–9</sup> These additives generate a weight increase (10–40%) for the battery electrode and extra steps to mix and combine those materials into a film form. And because this mixture is an inhomogeneous blend of carbon black, binders, and nanoparticles, the diffusion paths of

the ions and electrons are unclear, and it is difficult to model and characterize. Moreover, the mixture impedes specific testing of the active materials' properties since the choice of additive significantly affects the overall electrochemical performance of a cell.<sup>10,11</sup> Another unrefined parameter of conventional batteries is the lack of well-defined sizes and shapes of the nanoparticles. It is generally known that a homogeneous composition and a monodisperse morphology is crucial to maximize the nanoscale advantages.<sup>12</sup> However, controlling the size distribution and morphology of nanoparticles used in Li-ion battery electrodes is not common. Polydispersed nanoparticles complicate the understanding of the reaction mechanisms since each particle has a different Li-ion diffusion length. Many studies have shown that the sizes and shapes of nanoparticles influence the electrochemical performance and, remarkably, indicate that controlling the size and shapes is the key in order to fully understand the nanomaterial systems for Li-ion batteries.<sup>13,14</sup>

Previously, binder-free (binderless) and carbon-free electrodes from nanomaterials, such as "nanowires" or "nanotubes", have been developed.<sup>2,15–18</sup> However, the use of nanoparticles has not yet been established for additive-free electrode films. Several reports demonstrate binderless battery electrodes with

**Received:** May 23, 2012

**Revised:** August 13, 2012



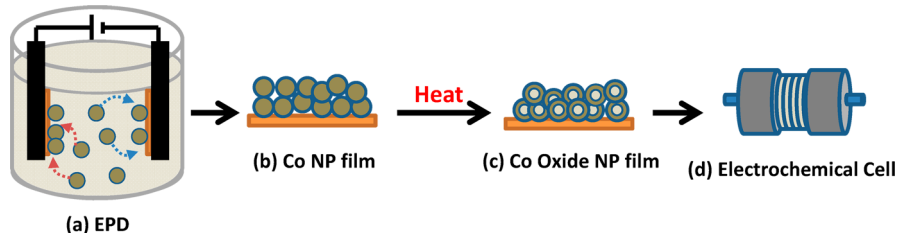


**Figure 1.** Schematic of process for fabrication of binderless, carbon-free nanoparticle film battery electrodes. (a) Electrophoretic deposition (EPD) apparatus for making cobalt nanoparticle (NP) films. A beaker with cobalt nanoparticles dispersed in a solvent. On each electrode, there is a copper collector, which acts as the substrate for the NP electrode. After the plates are immersed in the NP solution, a voltage is applied to the plates. The voltage induces cobalt NP deposition on both electrodes. (b) The Co NP film formed on copper current collector is calcinated at 200 °C in air and become (c) cobalt oxide NP film. (d) Finally, this film is assembled into an electrochemical cell.

nano<sup>19–22</sup> however, their films contain carbon-based conductive materials such as carbon nanotubes,<sup>19,20</sup> or form a hybrid with carbon, creating a conductive matrix.<sup>21,22</sup> These additive carbon materials do not contribute to the actual battery performance or show only limited capacity. A few reports exhibit electrodes without binders and free of conductive materials<sup>23,24</sup> but their materials are not “nanosized”, and thus do not benefit from any possible nanosize advantages.<sup>13,25</sup> There are only a few reports that show additive-free “nanoparticle” electrodes for lithium ion battery. Lee et al. showed binderless and carbonless nanoparticle-like films for Li-ion battery electrode however the particles are polydisperse and require a high temperature (~1400 °C) and a special instrument, hot-wire chemical vapor deposition, in order to build the nanoparticle electrode film.<sup>26</sup> Finke et al. demonstrated electrochemical deposition of Bi from an acidic bath of Bi solution, forming a nanoparticle film without additives, however the particles are not monodisperse and the battery does not show cyclability.<sup>27</sup> Additive-free, electrode films of nanoparticles (NPs) have not been well-developed, especially for colloidally synthesized NPs.

To harness the technologically important properties of nanoparticles, the particles need to be assembled in high-density films, devoid of their stabilizing organic ligands; the latter is essential if the film’s charge conductivity is important like in battery electrodes, flat panel displays, and in solar cells. Conventional self-assembly methods, for example, drop cast and slow solvent evaporation, result in incoherent films with voids and cracks that lack in mechanical strength and do not permit strong interparticle charge transfer.<sup>28</sup> An alternative is to use electric-field-assisted deposition or electrophoretic deposition (EPD). In the simplest scheme of EPD, a DC voltage is applied between two electrodes in a parallel plate capacitor configuration submerged in a nanoparticle solution. The particles are attracted to the electrodes simply by the Coulomb force, since many nanoparticle systems have surface facets and defects and are liable to be electrically charged.

EPD is a widely used technique to make coatings and thin films and has gained worldwide acceptance for a variety of applications such as automotive, appliance, and general industrial coatings. Advantages of EPD are high adherence and high density of the coating, homogeneity, and throw power. Complex shaped objects, for example, taps, fasteners, and metal cones, have been EPD coated for industrial applications due to EPD’s high throw power.<sup>29–31</sup> Wires of kilometer length have been coated for use in superconductivity.<sup>32</sup>

Application of EPD for assembling nanoparticles is relatively new. Giersig et al. have prepared ordered two-dimensional gold

colloid lattices on carbon-coated copper TEM grids by EPD.<sup>33</sup> Yeh et al. have deposited ordered colloidal aggregates of 2 μm diameter polystyrene beads.<sup>34</sup> Wong et al. have used the method to deposit 3–5 nm diameter ZnO nanocrystals on ITO electrodes.<sup>35</sup> Islam et al. have shown that EPD results in smooth, large area, almost defect-less CdSe nanoparticle films of high density, and that the interparticle interaction between the neighboring particles and between the electrode (current collector) and the particles in the EPD films is different than that of drop cast films.<sup>36,37</sup> Islam et al. have argued that by removing a controlled fraction of the organic ligands from the (inorganic) nanoparticle surface it is possible to simultaneously ensure the stabilization of the particles in the organic solvents and their chemical bonding to a metal electrode during EPD.<sup>37,38</sup> This last point was our impetus in fabricating Li-ion battery electrodes using EPD since high-quality dense nanoparticle films with built-in charge transfer pathways is the key to high battery rate capacity, cyclability, and longevity.

In this paper, we show how to construct a nanoparticle Li-ion battery electrode by using electrophoretic deposition of monodisperse nanoparticles without the use of binders or carbon black. To obtain monodisperse particles we synthesize cobalt nanoparticles through organic-phase colloidal nanocrystal synthesis methods, which are known to provide well-controlled shapes and sizes through the use of surfactant ligands.<sup>39</sup> The cobalt nanoparticles are assembled into films through EPD and then oxidized in air, leading to a hollow  $\text{Co}_3\text{O}_4$  nanoparticle film (Figure 1), which is mechanically very robust. We have found that use of EPD to form the binderless, carbon-free films results in good electrical connectivity, while the commonly used drop-casted films of the same particles, calcinated under identical conditions have poor electrical contact and poor battery performance. This EPD film also shows better mechanical stability and comparable electrochemical performance to the slurry coating film prepared by conventional methods. These additive-free  $\text{Co}_3\text{O}_4$  nanoparticle films show high gravimetric capacity compared to the theoretical capacity value and low degradation over many charge/discharge cycles. Additionally the volumetric capacity (>2100 mAh/cm<sup>3</sup>), based on the volume of  $\text{Co}_3\text{O}_4$  nanoparticle films, is 2.5 times higher than graphite (~800 mAh/cm<sup>3</sup>) and higher than other nanomaterials previously reported. To our knowledge, this is the first nanoparticle-film battery electrode made without using binders and carbon black additives to show very high gravimetric (>830 mAh/g) and volumetric capacities (>2100 mAh/cm<sup>3</sup>) even after 50 cycles.

The  $\epsilon$ -Co nanoparticle (NP) synthesis follows standard procedures.<sup>40</sup> A  $\text{N}_2$  flushed flask is filled with TOPO (0.1 g). After adding 0.09 g (0.32 mmol) of oleic acid dissolved in 12

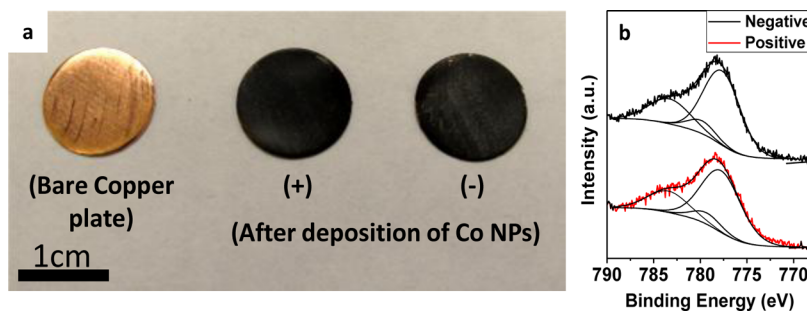


**Figure 2.** EPD-formed nanoparticle film. (a) Photograph of bare copper plate before NP deposition (left) and after deposition on (center) positive electrode and (right) negative electrode, which shows a thick, black NP film. (b) High-resolution Co 2p<sub>3/2</sub> XPS spectra of Co EPD film formed on positive (red line) and negative (black line) electrode.

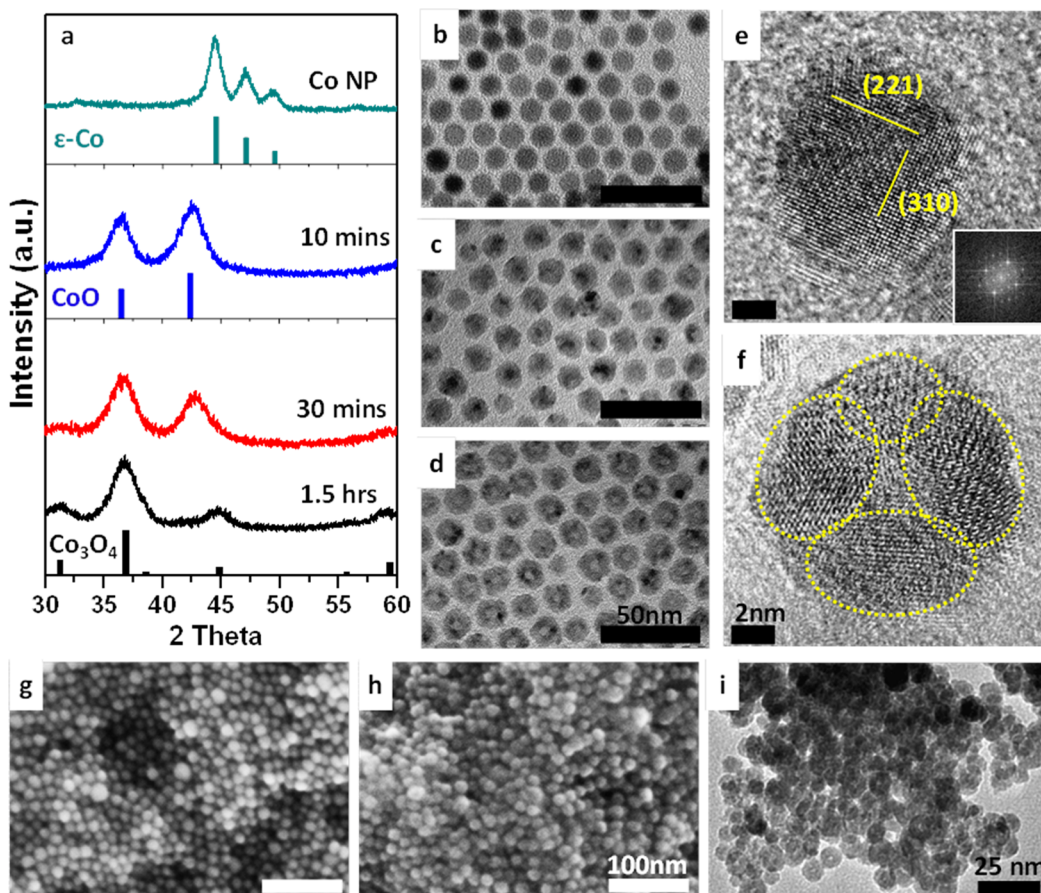


**Figure 3.** Materials characterization of EPD-formed nanoparticle electrodes. (a) XRD spectra of the samples from as-synthesized Co NPs to two phases of cobalt oxide through calcination at 200 °C in air. The green, blue, and black vertical bars correspond to references of ε-Co,<sup>46</sup> CoO (JCPDS No. 48-1719), and Co<sub>3</sub>O<sub>4</sub> (JCPDS No. 42-1467) phases, respectively. The 30 min oxidation sample is mixed phases of CoO and Co<sub>3</sub>O<sub>4</sub>. The 1.5 h sample is fully converted to Co<sub>3</sub>O<sub>4</sub>. TEM images of (b) as synthesized ε-Co NPs, (c) NPs calcinated for 30 min at 200 °C, and (d) NPs calcinated for 1.5 h at 200 °C. XRD indicates the phase of samples shown in d is the desired Co<sub>3</sub>O<sub>4</sub>. (e) HRTEM image and FFT (inset) of samples shown in b (ε-Co NP) and (f) HRTEM image of samples shown in d. (Co<sub>3</sub>O<sub>4</sub>) Yellow dotted circles in (f) indicate each crystalline regions of polycrystalline shell. Scale bar is 50 nm in b, c, and d, and 2 nm in e and f. (g,h) SEM images of EPD film: (g) before and (h) after oxidation shows dense network of NPs that should provide good electrical conducting pathways. (i) TEM image of NPs scraped off from oxidized EPD film. Hollow particles are evident in these films. Scale bar is 100 nm for g and h and 25 nm for i.

mL of 1,2-dichlorobenzene, the solution is heated. When the temperature of the solution reaches 180 °C, 0.52 g (1.52 mmol) of Co<sub>2</sub>(CO)<sub>8</sub> dissolved in 4 mL of 1,2-dichlorobenzene is quickly injected. After the reaction progresses for 5 min, the heating mantle is removed and the reaction solution is quenched in a water bath. The cobalt NPs are purified by adding ethanol and centrifuged. The supernatant is removed, and the NPs are redispersed in hexanes. This precipitation/

redisposition process is performed twice overall. Generally, additional washing leads to more charges on the NPs, which is important for the electric deposition process.<sup>41</sup> Colloidal ε-Co NPs are assembled onto a film through electrophoretic deposition (EPD). As shown in Figure 1, a copper current collector plate is attached to a stainless steel electrode plate for each polarity (+ and -). These two copper plates are facing each other and separated by 2 mm. The electrodes are

immersed in a solution of concentrated NP (0.1–1 mg/mL), dispersed in a solvent. A DC voltage (~150–600 V) is then applied to these electrodes. Once the voltage is applied a NP film forms on the electrodes and the NP solution turns from dark to clear. Deposition proceeds until the NP solution is very clear (~10 to 30 min depending on concentration and voltage). A film is formed on both the positive electrode and negative electrode. Figure 2a clearly shows the black NP film after the deposition of NPs. The film on the positive electrode is generally slightly thicker than that of the negative electrode (~20–80%), which indicates that more particles are negatively charged in the solvent. The thickness of the films can be made to be a few hundreds of nanometers to a few micrometers by controlling the concentration and deposition time. Generally, the polarities of these two electrodes are reversed several times during deposition in order to get a similar thickness on both electrodes.

To compare the chemistry of the nanoparticle films formed on the opposite electrodes during EPD, XPS (X-ray photo-electron spectroscopy) with monochromated aluminum K-alpha X-rays (1486.6 eV) is utilized. Figure 2b shows Co 2p<sub>3/2</sub> XPS spectra of the samples fabricated on positive electrode (red line) and negative electrode (black line). Both spectra exhibit the strong Co 2p<sub>3/2</sub> peak around 778.4 eV confirming that both samples contain Co<sup>0</sup> as their major component. Each spectrum is deconvoluted to three Gaussian peaks that correspond to Co<sup>0</sup> at 778.1 eV and Co<sup>2+</sup> at 780.2 and 783.9 eV (shakeup satellites)<sup>42,43</sup> indicating the surface oxidation of CoO phase. Both samples show the identical amount of surface oxidation and energy shifts, confirming that the opposite polarity of e-field during EPD does not influence the chemistry of the NPs.

To form the cobalt oxide used as an electrode in Li-ion batteries the  $\epsilon$ -cobalt NP films are oxidized in air at 200 °C (see Figure 1). XRD data show that the NPs transform from  $\epsilon$ -cobalt to two phases of cobalt oxide through the calcination process in air (Figure 3a). The Co<sub>3</sub>O<sub>4</sub> phase is the useful phase for lithium ion battery anodes since it has one of the highest theoretical capacities among metal oxides.<sup>1,8,44</sup> The XRD peaks of the initial cobalt NPs match well with the reference standard peaks (Figure 3a, green bars) of the  $\epsilon$ -cobalt phase, which is the common phase for cobalt metal in NPs.<sup>40,45,46</sup> After heating the Co NP film in the furnace at 200 °C for 10 min, Co NPs oxidize and the major phase becomes CoO. The XRD spectrum of the sample calcinated for 10 min shows broader peaks than those of  $\epsilon$ -Co NPs, which indicates the decreased grain size and reduced long-range order from the oxidation. Through further heating, the CoO NPs begin to transform to the Co<sub>3</sub>O<sub>4</sub> phase. The XRD pattern of the sample that is calcinated for 30 min at 200 °C shows two peaks around 37 and 43°, which correspond to the strongest diffraction planes for Co<sub>3</sub>O<sub>4</sub> and CoO phase, respectively. After a total heating time of 1.5 h, the CoO strongest peak is no longer detected and the NPs have transformed into Co<sub>3</sub>O<sub>4</sub> phase. Longer oxidation times do not lead to other oxygen rich phases, such as Co<sub>2</sub>O<sub>3</sub> (see Supporting Information Figure S1).

Comparing the air oxidation of cobalt to solution-phase oxidation we note that, unsurprisingly, the air calcination process more effectively converts the metal to the oxide phases. In the solution-phase method, the Co NPs react with an O<sub>2</sub>/Ar mixture gas for 3 h at 455 K and result in only the CoO phase.<sup>47</sup>

TEM characterization of the morphological evolution during the transformation from cobalt to cobalt oxides show

monodisperse  $\epsilon$ -Co NPs that transform into hollow final products. The studies were conducted by depositing  $\epsilon$ -Co NPs on a carbon-coated TEM grid and heating the grid to 200 °C in air. The initial  $\epsilon$ -Co NPs are a monodisperse spherical shape and monodisperse size (size: 9.5 nm, SD 8%) (Figure 3b). After 30 min heating at 200 °C, the NPs (Figure 3c) have a dark center that is commonly seen at the onset of the nanoscale Kirkendall effect as the transformation is initiated and a shell begins to develop.<sup>45,47</sup> The nanoscale Kirkendall effect is due to the asymmetric diffusion rates of atoms and ions in a material and results in hollow nanoparticles. After heating for 1.5 h, the sample converts to Co<sub>3</sub>O<sub>4</sub> and the NPs exhibit the Kirkendall hollowing with bigger NP size (size: 13.4 nm, SD 9%) (Figure 3d). Through this transition progression, the single crystalline cobalt NPs transforms to polycrystalline hollow NPs, as confirmed by HRTEM (Figure 3e,f). Scherrer analysis of the grains also shows a decrease in crystal size from ~10 nm in initial cobalt NP to ~4.3 nm in Co<sub>3</sub>O<sub>4</sub> NP (Figure 3a).

SEM images of the films show a random network of deposited particles that increases in density after the oxidation process. The Co NP film formed by EPD shows an assembly of NPs separated by surfactant ligands (Figure 3g). After oxidation for 1.5 h at 200 °C, discrete NPs are still evident in the film, but the particles now form a denser network due to the decrease in interparticle spacing (Figure 3h). TEM samples of the interior were prepared to ensure that the NPs in the interior of the film are similar to those shown on the surface with the SEM images, that is, not sintered and exist as discrete particles. TEM results of the NPs from oxidized film show aggregation, but the NPs are not sintered into bulk material (Figure 3i).

These EPD films show very rigid contact between the NP film and the copper current collector for both cobalt NP films and the films after oxidation. Both the EPD as-deposited cobalt film and the oxidized film are no longer soluble in typical NP solvents such as hexane, even with an ultrasonication procedure. This excellent physical connectivity property might be the source of good electrical conducting pathways.

Elemental analysis of carbon atoms was performed for both the initial cobalt nanoparticles and the cobalt oxide nanoparticles in order to investigate the change of the organic surfactant ligands that are initially present on the surface of the cobalt nanoparticles. The elemental analysis is performed for carbon by high-temperature combustion followed by IR detection. The initial carbon weight percent of cobalt NP sample was about 6.7 wt % and this carbon weight significantly decreased to 0.84 wt % after the oxidation of the sample at 200 °C in air, indicating that most of the organic components are burned off through the heating process. The 0.84 wt % of carbon is significantly less than that is required for monolayer coverage of carbon on the 14 nm sized NPs.

Thickness measurements show a contraction of the volume after oxidation (Table 1). Three cobalt NP films with different

**Table 1. Thickness and Volume Analysis of Three Samples with Different Thicknesses**

sample	thickness		volume change after oxidation	density of Co <sub>3</sub> O <sub>4</sub> NP Film
	cobalt NP film	cobalt oxide NP film		
1	465 nm	347 nm	25% reduction	2.72 g/cm <sup>3</sup>
2	1001 nm	725 nm	28% reduction	2.12 g/cm <sup>3</sup>
3	1497 nm	1136 nm	24% reduction	2.23 g/cm <sup>3</sup>

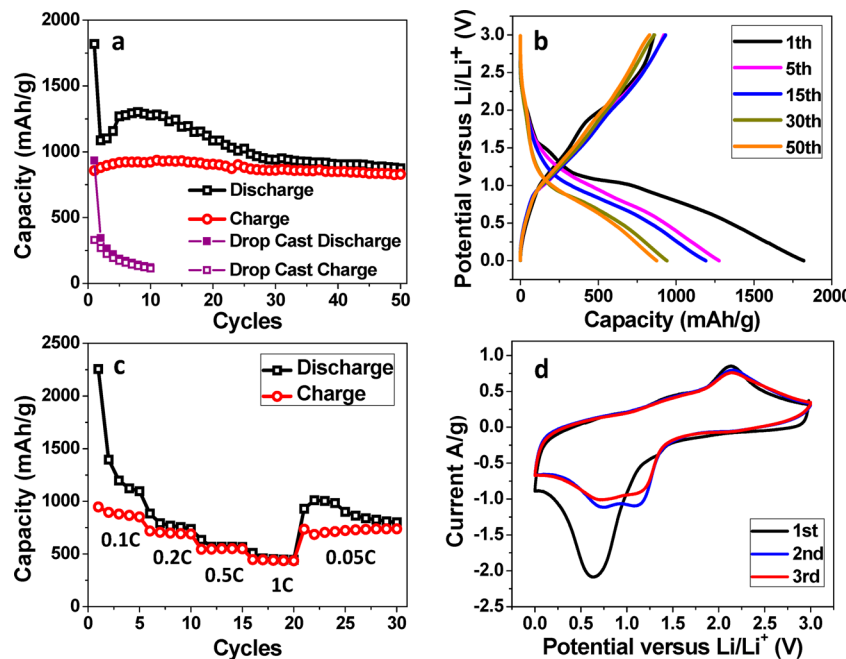


**Figure 4.** Electrochemical performance of EPD  $\text{Co}_3\text{O}_4$  NP films without carbon black and polymeric additives. (a) Capacity retention at C/20 rate showing the charge (red circles) and discharge (black squares). The purple solid squares and purple open squares show the discharge and charge capacities of drop casted film, respectively. (b) Galvanostatic charge–discharge curves and (c) cycling performance at various current rates showing charge (red circles) and discharge (black squares). (d) Cyclic voltammetry at 50 mV/s rate.

thicknesses, 470, 1000, and 1500 nm, were prepared through EPD. Surprisingly, all the samples showed about a 25% reduction in thickness after oxidation despite the increased particle sizes from the Kirkendall hollowing (Table 1). Even when the shrinkage of the volume due to the organic ligands elimination is considered, this 25% reduction is surprising because the NP size actually increases about 40% during oxidation and the density of  $\text{Co}_3\text{O}_4$  ( $6.11 \text{ g/cm}^3$ ) is also lower than that of  $\epsilon\text{-Co}$  ( $8.64 \text{ g/cm}^3$ ). This contraction of the film implies that the NPs are filling the porous spaces and settling on more stable sites during oxidation process.

Our EPD-formed  $\text{Co}_3\text{O}_4$  NP films show higher density than the tap density of a mixture of the same  $\text{Co}_3\text{O}_4$  NPs with carbon black and polyvinylidene fluoride (conventional slurry method):  $2.12\text{--}2.72 \text{ g/cm}^3$  for the EPD films versus  $1.76 \text{ g/cm}^3$  for the mixture and its dried slurry, based on the  $\text{Co}_3\text{O}_4$  NP mass. The EPD nanoparticle films also show higher density than the  $\text{Co}_3\text{O}_4$  NP dried slurry mixture pressed under 160 MPa ( $2.18 \text{ g/cm}^3$ ) (see Supporting Information).

The electrochemical performance of these additive-free  $\text{Co}_3\text{O}_4$  nanoparticle films formed by EPD were tested by using the films as a working electrode in a Swagelok-type electrochemical cells. The cells were completed by using Li foil as the counter electrode, 1 M LiPF<sub>6</sub> in a 50:50 w/w mixture of ethylene carbonate and diethyl carbonate as an electrolyte, and a polypropylene separator (Celgard 2400). Figure 4a shows the charge/discharge capacity of the film through 50 cycles at C/20 rate considering C as 900 mAh/g. Even after 50 cycles of charge/discharge the capacity is retained near the theoretical capacity (890 mAh/g), much higher than graphite (372 mAh/g) that is commercially used as the anode material of Li-ion batteries. However, the working voltage of our  $\text{Co}_3\text{O}_4$  EPD film is higher than that of graphite. Figure 4b shows the galvanostatic discharge (lithiation) – charge (delithiation) curves at C/20 that exhibits high capacity for the first discharge

(1820 mAh/g) and decreased throughout cycles. This huge reduction in capacity after the first cycle is due to characteristic irreversible reactions.<sup>12,44</sup> Additionally, there is a small capacity contribution from copper oxide thin layer of copper current collector which might be formed during oxidation. As a control experiment, an electrochemical measurement was conducted with a bare copper plate (no NP film) that was treated with the same oxidation process. This heat-treated copper plate shows a capacity of about 240 mAh/g for the first discharge, but drops to 30 mAh/g for the second cycle, and becomes negligible after several cycles indicating that there is a small contribution to the overall capacity only for first few cycles (see Figure S2). Figure 4c shows the cycling performance at various current rates. This result reveals the excellent recovery of these novel films after 20 cycles of high current rates. However, at a low current rate (C/20) the samples show discharge capacity increasing for the first several cycles that indicates additional reactions for the low current rate (Figure 4a,c). Insight into the redox reaction is given (Figure 4d) by a cyclic voltammetry (CV) measurement with lithium as a counter electrode at 0.5 mV/s. The peaks of the CV cycle for the EPD films are well matched with other  $\text{Co}_3\text{O}_4$  nanomaterials.<sup>8,12,48</sup> The first cycle of CV shows broad oxidation peaks around 1.5 and 2.15 V and one reduction peak at 0.63 V that becomes two peaks in the second cycle around 1.26 and 0.84 V.

In order to understand how our EPD films differ from films formed by other techniques, we compared our EPD method against drop-casted films and conventional slurry-coated films with polymeric binder and carbon black. Drop-casting is a widely used method to form NP films.<sup>49,50</sup> The drop-cast film of NPs was prepared by depositing cobalt nanoparticles dispersed in solvents with different boiling points (bp) such as hexane (low bp) and tetrachloroethylene (high bp) onto a substrate by evaporation of solvents and then calcinating the particles under identical conditions (200 °C for 2 h in air). The

conventional film is prepared by mixing  $\text{Co}_3\text{O}_4$  NPs with PVDF (polyvinylidene fluoride) and carbon black (see Supporting Information). The total amount of NPs deposited through drop-casting and the conventional film is controlled to be that of the EPD films. We have investigated the mechanical stability of all three samples with  $\text{Co}_3\text{O}_4$  nanoparticles: (1) NP films assembled through EPD, (2) NP films formed by drop-casting, and (3) NP films with PVDF and carbon black prepared through conventional methods. A bending test and an adhesion test were carried out to examine the mechanical firmness. Bending experiments were carried out up to a 0.35 cm radius of curvature. All samples do not show any noticeable cracking (Supporting Information Figure S3). Figure 5a shows the bent

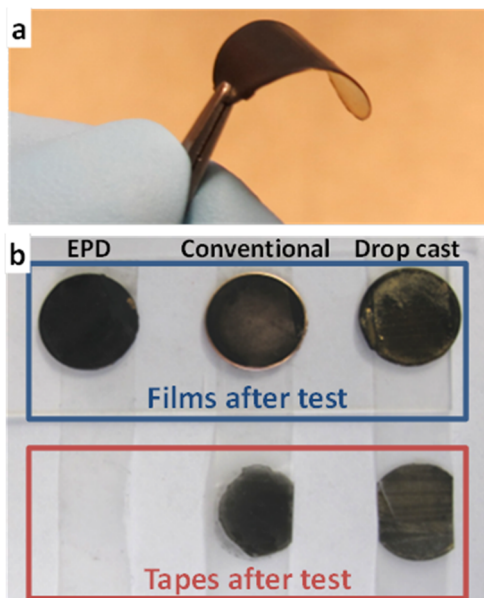


**Figure 5.** Mechanical stability test of  $\text{Co}_3\text{O}_4$  nanoparticle films. (a) EPD film bends without any noticeable cracks. (b) Scotch tape method is used for adhesion test. Films in the blue box show the electrodes after the adhesion test. The films are prepared on copper plates by EPD (left), the conventional method (center), and drop-casting (right). The tapes after the test are shown in red box. The tape tested for EPD film (left) shows no noticeable nanoparticles while those for conventional (center) and drop casting (right) film exhibit a significant amount of black film that has de-adhered from the electrodes.

EPD NP film. An adhesion test was also used to evaluate the mechanical rigidity. Scotch tape was well-attached to the sample films and pulled off (see Supporting Information). Surprisingly, the EPD film is very stable while the other films were partially de-adhered by the tape. This is shown in Figure 5b; after the tapes were removed the conventional and drop cast samples clearly show the black NPs removed from the copper plate (Figure 5b, top) and the NPs sticking to the tape (Figure 5b, bottom). The EPD film, however, exhibits little to none de-adhesion of NPs from the adhesion test. This excellent mechanical stability might provide a critical benefit for building a battery without additives.

Electrochemical performance was also measured for drop-casted and conventional nanoparticle films. The  $\text{Co}_3\text{O}_4$  NP films formed by drop-casting and by conventional methods were assembled into a Swagelok-type electrochemical cell and measurements similar to those on the EPD films were carried

out. No additional polymer binders and carbon black were added to the drop-cast sample as EPD film. Cyclic voltammetry (CV) measurements of drop-casted films with lithium as a counter electrode displays many spikes due to poor contacts between NPs and the copper current collector, especially during the deintercalation of lithium ions from cobalt oxide film (Supporting Information Figure S4). This poor contact deteriorates even more as charge/discharge cycles are carried out, while the EPD film shows smooth reduction and oxidation curves over all cycles. The galvanostatic measurement also reveals that the EPD films exhibit much better cycle performance than drop-casted films at C/20 rate (Figure 4a). In general, most of the drop-casted films (>80%) fail to show the reasonable data without any spikes (see Supporting Information Figure S5) and the cycle performance of the remaining 20% exhibit very poor capacity retention. EPD films, however, show only a small decrease of a capacity after cycling. This result explains why polymeric binder and carbon black are needed in all other NP battery electrodes when the NPs are simply placed (drop-cast) on a current collector. The conventional slurry coated film shows similar cyclability through 50 cycles without any significant difference compared to the EPD film's performance (Supporting Information Figure S6).

The volumetric capacity is calculated based on the volume of the cobalt oxide film formed through EPD and oxidation process. The density of our cobalt oxide EPD film is 2.12–2.72 g/cm<sup>3</sup> which means overall packing factor of the film is about 0.35–0.45 since the density of  $\text{Co}_3\text{O}_4$  phase is 6.11 g/cm<sup>3</sup>. Therefore, for the high gravimetric capacity samples (890 mAh/g, measured at a low current rate) the volumetric capacity is 2100–2500 mAh/cm<sup>3</sup>. This volumetric capacity is much higher than graphite, which is about 800 mAh/cm<sup>3</sup><sup>51</sup> and also higher than other reported nanomaterials.<sup>15,52,53</sup> For a more accurate determination of volumetric capacity, the volume expansion and contraction during discharge/charge cycles will be taken into account in future studies. Future improvements in packing factor are expected from using a slower EPD process (low V and longer deposition time) to create a higher density of NP films. Preliminary studies indicate that varying the deposition conditions can lead to denser films (~20%), but further study is necessary.

To understand the dependence on film thicknesses and EPD applied voltages, further experiments were carried out in this parameter space. To represent the cyclability, the charge capacity of the 10th cycle of each sample is chosen. Figure 6 shows the correlation between the cycle performance and thicknesses of films at different EPD voltages. The black solid squares and red solid squares represent the 10th cycle charge capacities at a C/20 rate for the 300 and 600 V EPD deposited samples, respectively. The open black squares, open red squares, and open blue squares display the 10th cycle capacities of the 300, 600, and 150 V samples, respectively, measured at C/10 rate for first 5 cycles and C/5 rate for last 5 cycles. This plot shows that the EPD voltage does not influence the cycle performance significantly within the range from 150 to 600 V. It however clearly shows that the battery capacity strongly depends on the film thickness. The capacity decreases when the film is thicker than 1  $\mu\text{m}$  and becomes less than 20% of the theoretical capacity for a 5  $\mu\text{m}$  thick sample. This thickness-dependent capacity indicates that the critical thickness of the film, in order to fully utilize battery performance, is 1  $\mu\text{m}$ . It is likely that this limit is governed by the limited electrical

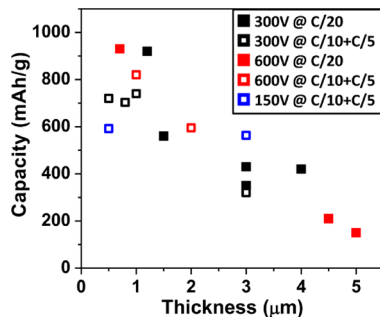


**Figure 6.** Relationship between average film thickness and the charge capacity for different applied voltages during EPD. Capacity was taken at 10th cycle. The black solid squares and red solid squares present 10th cycle capacities at C/20 rate for films assembled at EPD voltages of 300 and 600 V, respectively. The open black squares, open red squares, and open blue squares show 10th cycle capacities of 300, 600, and 150 V samples, respectively, measured at C/10 rate for first 5 cycles and C/5 rate for remaining 5 cycles.

conductivity of the oxide particles. Films with higher packing factors should improve the range of peak-performing thicknesses since higher packing implies additional connectivity pathways between NPs.

Because of the absence of binders and carbon black, we can study the morphology evolution during cycles. After the electrochemical measurements were completed, the Swagelok cells were disassembled and the EPD films were cleaned with diethylene carbonate, ethanol, and hexane in order to remove electrolyte residues. The samples were then scraped off from the copper current collector and put on TEM grids. Figure 7a shows the TEM image of aggregated small NPs (size:  $\sim$ 5–10 nm) after first lithiation process, which reveals that the NPs are no longer individual hollow NPs. This implies that the polycrystalline hollow NPs break into smaller NPs during lithiation. Also after delithiated, NPs are even smaller (size: about 5 nm) (Figure 7b). These small ( $\sim$ 5 nm) NPs remain

after 30 cycles of lithiation/delithiation cycle (Figure 7c). These results suggest the evolution of the NPs during battery operation (Figure 7d): the initial cobalt oxide NPs are polycrystalline with hollow structure; during the first lithiation step, the polycrystalline hollow NPs break into several pieces, possibly along the grain boundaries, and these small NPs can reversibly accommodate lithium ions through cycles. Many nanoparticle systems have been used for size dependent electrochemical properties and each case shows different sizes for the best performance.<sup>1,13,54</sup> In the  $\text{Co}_3\text{O}_4$  NP system, 5–10 nm may be a stable size for reversible lithiation and delithiation without pulverization.

We have demonstrated a new method to build high-capacity, additive-free nanoparticle films for Li-ion battery electrodes, eliminating the need for polymeric binders and conductive carbon materials. Removing additives is an effective means to reduce the weight and volume of batteries. Our method employs colloidal synthesis techniques to produce spherical, monodisperse cobalt metal NPs, which are solution-processable. The critical solution-processing technique that we use to obtain good battery performance for the NP films is EPD. EPD binds the metal NPs to the surface of the electrode and to each other in an assembly, which is subsequently converted to  $\text{Co}_3\text{O}_4$  NPs with a polycrystalline hollow structure.

Our cobalt oxide NP films formed without any binders and carbon black show excellent cyclability at low current. This EPD film exhibits superior mechanical stability to other films fabricated by drop-casting or through conventional slurry methods. The electrochemical properties are optimized when the film is 1  $\mu\text{m}$  thick. By scraping off the NPs from current collectors, the morphology change is studied after lithiated and delithiated. A stable particle size of 5–10 nm is retained through the lithiation/delithiation cycling.

Because of the absence of additive materials, this method can provide a good template system to investigate the physical mechanisms and understand the reactions during charge/discharge. This system provides opportunities to utilize

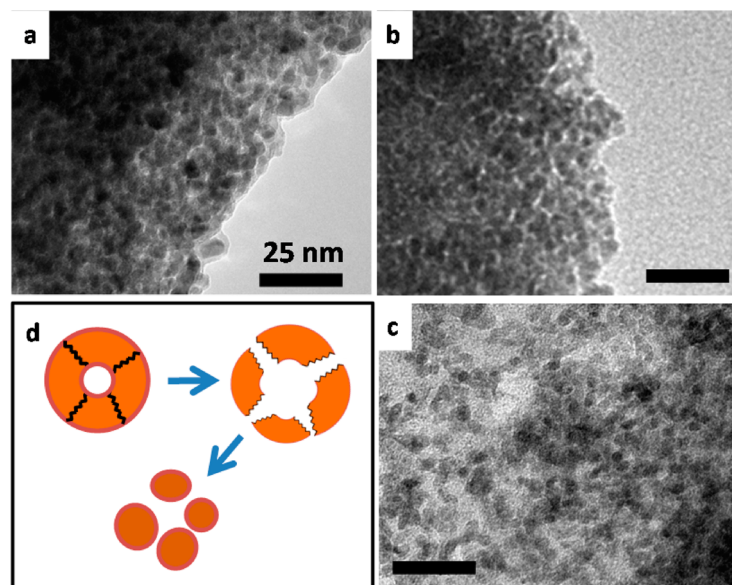


**Figure 7.** TEM images and schematic of nanoparticles through lithiation/delithiation process. (a) After lithiation, (b) after 1 lithiation/delithiation cycle, and (c) after 30 cycles. The size of the particles are between 5 and 10 nm for (a) and  $\sim$ 5 nm for (b) and (c). (d) Schematic of the evolution of NPs during lithiation. Initial cobalt oxide NP is polycrystalline with hollow structure. During the lithiation process, the NP breaks into several particles and finally become individual NPs.

colloidal NPs for battery electrodes in a simple and robust manufacturing process.

## ■ ASSOCIATED CONTENT

### Supporting Information

Additional information and figures. This material is available free of charge via the Internet at <http://pubs.acs.org>.

## ■ AUTHOR INFORMATION

### Corresponding Author

\*E-mail: rdr82@cornell.edu.

### Notes

The authors declare no competing financial interest.

## ■ ACKNOWLEDGMENTS

We thank the Abruña group and Archer group for their helpful suggestions for battery measurements and analysis, and Jon Shu for help with XPS data and analysis. We thank Denzel Bridges and Diana Gooding for their help with film fabrication. This work was supported in part by the Cornell Center for Materials Research (CCMR) with funding from the Materials Research Science and Engineering Center program of the National Science Foundation (cooperative agreement DMR 1120296). D.H.H. was primarily supported by the Energy Materials Center at Cornell (EMC<sup>2</sup>), an Energy Frontier Research Center funded by the U.S. Department of Energy, Office of Science, Office of Basic Energy Science under Award Number DE-SC0001086. This publication is based on work supported in part by Award No. KUS-C1-018-02, made by King Abdullah University of Science and Technology (KAUST).

## ■ REFERENCES

- (1) Poizot, P.; Laruelle, S.; Gruegeon, S.; Dupont, L.; Tarascon, J. M. *Nature* **2000**, *407* (6803), 496–499.
- (2) Chan, C. K.; Peng, H. L.; Liu, G.; McIlwrath, K.; Zhang, X. F.; Huggins, R. A.; Cui, Y. *Nat. Nanotechnol.* **2008**, *3* (1), 31–35.
- (3) Chen, J.; Xu, L.; Li, W.; Gou, X. *Adv. Mater.* **2005**, *17* (5), 582–586.
- (4) Taberna, P. L.; Mitra, S.; Poizot, P.; Simon, P.; Tarascon, J. M. *Nat. Mater.* **2006**, *5* (7), 567–573.
- (5) Cabana, J.; Monconduit, L.; Larcher, D.; Palacín, M. R. *Adv. Mater.* **2010**, *22* (35), E170–E192.
- (6) Park, M.-H.; Kim, K.; Kim, J.; Cho, J. *Adv. Mater.* **2010**, *22* (3), 415–418.
- (7) Gao, J.; Lowe, M. A.; Abruña, H. c. D. *Chem. Mater.* **2011**, *23* (13), 3223–3227.
- (8) Wu, Z.-S.; Ren, W.; Wen, L.; Gao, L.; Zhao, J.; Chen, Z.; Zhou, G.; Li, F.; Cheng, H.-M. *ACS Nano* **2010**, *4* (6), 3187–3194.
- (9) Wang, H.; Cui, L.-F.; Yang, Y.; Sanchez Casalongue, H.; Robinson, J. T.; Liang, Y.; Cui, Y.; Dai, H. J. *J. Am. Chem. Soc.* **2010**, *132* (40), 13978–13980.
- (10) Kovalenko, I.; Zdyrko, B.; Magasinski, A.; Hertzberg, B.; Milicev, Z.; Burtovy, R.; Luzinov, I.; Yushin, G. *Science* **2011**, *334* (6052), 75–79.
- (11) Jin, B.; Gu, H.-B.; Kim, K.-W. *J. Solid State Electrochem.* **2008**, *12* (2), 105–111.
- (12) Nam, K. T.; Kim, D.-W.; Yoo, P. J.; Chiang, C.-Y.; Meethong, N.; Hammond, P. T.; Chiang, Y.-M.; Belcher, A. M. *Science* **2006**, *312* (5775), 885–888.
- (13) Kim, C.; Noh, M.; Choi, M.; Cho, J.; Park, B. *Chem. Mater.* **2005**, *17* (12), 3297–3301.
- (14) Chen, J. S.; Zhu, T.; Hu, Q. H.; Gao, J.; Su, F.; Qiao, S. Z.; Lou, X. W. *ACS Appl. Mater. Interfaces* **2010**, *2* (12), 3628–3635.
- (15) Chockla, A. M.; Harris, J. T.; Akhavan, V. A.; Bogart, T. D.; Holmberg, V. C.; Steinhagen, C.; Mullins, C. B.; Stevenson, K. J.; Korgel, B. A. *J. Am. Chem. Soc.* **2011**, *133* (51), 20914–20921.
- (16) Li, Y.; Lv, X.; Li, J. *Appl. Phys. Lett.* **2009**, *95* (11), 113102–3.
- (17) Li, C. C.; Li, Q. H.; Chen, L. B.; Wang, T. H. *J. Mater. Chem.* **2011**, *21* (32), 11867–11872.
- (18) Wu, H.; Chan, G.; Choi, J. W.; Ryu, I.; Yao, Y.; McDowell, M. T.; Lee, S. W.; Jackson, A.; Yang, Y.; Hu, L.; Cui, Y. *Nat. Nanotechnol.* **2012**, *7* (5), 310–315.
- (19) Zhang, H.-X.; Feng, C.; Zhai, Y.-C.; Jiang, K.-L.; Li, Q.-Q.; Fan, S.-S. *Adv. Mater.* **2009**, *21* (22), 2299–2304.
- (20) Ban, C. M.; Wu, Z. C.; Gillaspie, D. T.; Chen, L.; Yan, Y. F.; Blackburn, J. L.; Dillon, A. C. *Adv. Mater.* **2010**, *22* (20), E145–149.
- (21) Jo, G.; Choi, I.; Ahn, H.; Park, M. J. *Chem. Commun.* **2012**, *48* (33), 3987–3989.
- (22) Sun, Y.; Hu, X.; Yu, J. C.; Li, Q.; Luo, W.; Yuan, L.; Zhang, W.; Huang, Y. *Energy Environ. Sci.* **2011**, *4* (8), 2870–2877.
- (23) Yao, Y.; McDowell, M. T.; Ryu, I.; Wu, H.; Liu, N.; Hu, L.; Nix, W. D.; Cui, Y. *Nano Lett.* **2011**, *11* (7), 2949–2954.
- (24) Lai, W.; Erdonmez, C. K.; Marinis, T. F.; Bjune, C. K.; Dudney, N. J.; Xu, F.; Wartena, R.; Chiang, Y.-M. *Adv. Mater.* **2010**, *22* (20), E139–E144.
- (25) Koo, B.; Xiong, H.; Slater, M. D.; Prakapenka, V. B.; Balasubramanian, M.; Podsiadlo, P.; Johnson, C. S.; Rajh, T.; Shevchenko, E. V. *Nano Lett.* **2012**, *12* (5), 2429–2435.
- (26) Lee, S.-H.; Kim, Y.-H.; Deshpande, R.; Parilla, P. A.; Whitney, E.; Gillaspie, D. T.; Jones, K. M.; Mahan, A. H.; Zhang, S.; Dillon, A. C. *Adv. Mater.* **2008**, *20* (19), 3627–3632.
- (27) Finke, A.; Poizot, P.; Guery, C.; Dupont, L.; Taberna, P.-L.; Simon, P.; Tarascon, J.-M. *Electrochim. Solid-State Lett.* **2008**, *11* (3), E5–E9.
- (28) Leatherdale, C. A.; Kagan, C. R.; Morgan, N. Y.; Empedocles, S. A.; Kastner, M. A.; Bawendi, M. G. *Phys. Rev. B* **2000**, *62* (4), 2669–2680.
- (29) Ryan, W.; Massoud, E. *Interceram* **1979**, *28* (2), 117–119.
- (30) Aveline, M. *Ind. Ceram.* **1966**, *581*, 28–31.
- (31) Ortner, M. *Plating* **1964**, *51* (9), 885.
- (32) Barraclough, M.; Bolton, N.; Collins, A.; Andrews, J. *IEEE Trans. Magn.* **1967**, *3* (3), 531–534.
- (33) Giersig, M.; Mulvaney, P. *Langmuir* **1993**, *9* (12), 3408–3413.
- (34) Yeh, S.-R.; Seul, M.; Shraiman, B. I. *Nature* **1997**, *386* (6620), 57–59.
- (35) Wong, E. M.; Searson, P. C. *Chem. Mater.* **1999**, *11* (8), 1959–1961.
- (36) Islam, M. A.; Herman, I. P. *Appl. Phys. Lett.* **2002**, *80* (20), 3823–3825.
- (37) Islam, M. A.; Xia, Y.; Telesca, D. A.; Steigerwald, M. L.; Herman, I. P. *Chem. Mater.* **2003**, *16* (1), 49–54.
- (38) Islam, M. A.; Xia, Y.; Steigerwald, M. L.; Yin, M.; Liu, Z.; O'Brien, S.; Levicky, R.; Herman, I. P. *Nano Lett.* **2003**, *3* (11), 1603–1606.
- (39) Yin, Y.; Alivisatos, A. P. *Nature* **2005**, *437* (7059), 664–670.
- (40) Puntes, V. F.; Krishnan, K. M.; Alivisatos, A. P. *Science* **2001**, *291* (5511), 2115–2117.
- (41) Gonzalo-Juan, I.; Krejci, A. J.; Dickerson, J. H. *Langmuir* **2012**, *28* (11), 5295–5301.
- (42) Li, H.; Liao, S. *J. Mater. Chem.* **2009**, *19* (29), 5207–5211.
- (43) Chen, Y.; Liew, K. Y.; Li, J. *Appl. Surf. Sci.* **2009**, *255* (7), 4039–4044.
- (44) Lou, X. W.; Deng, D.; Lee, J. Y.; Feng, J.; Archer, L. A. *Adv. Mater.* **2008**, *20* (2), 258–262.
- (45) Ha, D.-H.; Moreau, L. M.; Bealing, C. R.; Zhang, H.; Hennig, R. G.; Robinson, R. D. *J. Mater. Chem.* **2011**, *21* (31), 11498–11510.
- (46) Dinega, D. P.; Bawendi, M. G. *Angew. Chem., Int. Ed.* **1999**, *38* (12), 1788–1791.
- (47) Yin, Y. D.; Rioux, R. M.; Erdonmez, C. K.; Hughes, S.; Somorjai, G. A.; Alivisatos, A. P. *Science* **2004**, *304* (5671), 711–714.
- (48) Gu, Y.; Jian, F.; Wang, X. *Thin Solid Films* **2008**, *517* (2), 652–655.

- (49) Talapin, D. V.; Murray, C. B. *Science* **2005**, *310* (5745), 86–89.
- (50) Yu, D.; Wang, C.; Guyot-Sionnest, P. *Science* **2003**, *300* (5623), 1277–1280.
- (51) Beaulieu, L. Y.; Larcher, D.; Dunlap, R. A.; Dahn, J. R. *J. Electrochem. Soc.* **2000**, *147* (9), 3206–3212.
- (52) Magasinski, A.; Dixon, P.; Hertzberg, B.; Kvít, A.; Ayala, J.; Yushin, G. *Nat. Mater.* **2010**, *9* (4), 353–358.
- (53) Yoon, S.; Jo, C.; Noh, S. Y.; Lee, C. W.; Song, J. H.; Lee, J. *Phys. Chem. Chem. Phys.* **2011**, *13* (23), 11060–11066.
- (54) Liu, X. H.; Zhong, L.; Huang, S.; Mao, S. X.; Zhu, T.; Huang, J. Y. *ACS Nano* **2012**, *6* (2), 1522–1531.